GRL

Supporting Information for

Snow reconciles observed and simulated phase partitioning and doubles cloud feedback

Grégory V. Cesana[1,2,] Andrew S. Ackerman[2], Ann M. Fridlind[2], Israel Silber[3] and Maxwell Kelley[2]

[1] Center for Climate Systems Research, Columbia University, New York, NY

[2] NASA Goddard Institute for Space Studies, New York, NY

[3] Pennsylvania State University, University Park, PA

Contents of this file

Text S1 to S5
Figures S1 to S11
Tables S1 to S3

Introduction

In this supporting information file, we provide additional details about:

- the uncertainty estimates used for the CALIPSO-GOCCP observations in text S1,
- GISS-ModelE3 description in text S2,
- how the lidar simulator was modified to account for precipitation along with additional modifications to improve consistency with NASA-GISS ModelE3 in text S3,
- the two case studies used the main manuscript in text S4,
- how the simulated cloud feedbacks are computed in text S5,
- figures that further support our main findings in figures S1-S11,
- the averaged cloud feedbacks for different NASA-GISS ModelE3 configurations in table S1-S2 and
- the list of CMIP models used in this study as well as their ECS.

Supplementary Texts

Text S1:

To derive an observational uncertainty estimate for the SCF as a function of temperature (liquid/[liquid+ice] cloud frequency), we use error estimates from a CALIPSO-GOCCP validation study against *in situ* aircraft measurements[16] as well as the undefined-phase cloud fraction. Cesana et al.(2016) show that the maximum disagreement fraction between CALIPSO-GOCCP and five *in situ* aircraft flights is ~ 20 % (their Table 3). We choose to apply this maximum disagreement fraction of 20 % uniformly to the CALIPSO-GOCCP cloud phase ratio although Cesana et al.[16] showed that the ice clouds in high and cold clouds were rarely misdiagnosed. In addition, we use the undefined-phase cloud fraction to derive a range of possible SCF as a function of the temperature by considering the undefined-phase clouds as being either all liquid or all ice. Finally, we assume that both uncertainty sources –from applying the 20 % disagreement fraction and from considering all undefined-phase clouds as being either liquid or ice– are independent and add them in quadrature to derive the final uncertainty estimate.

Text S2:

In brief, GISS-ModelE3 uses a diagnostic determination of cloud fraction as a function of grid-mean moisture and a condition-dependent sub-grid variance expressed as a threshold grid-mean relative humidity (RH) for cloud formation. The stratiform liquid and ice cloud fractions are obtained using Smith (1990) and Wilson and Ballard (1999) probability density function (PDF) schemes. The stratiform cloud microphysics treatment is based on a modified two-moment microphysics scheme with prognostic precipitation (Gettelman and Morrison, 2015), in which cloud water and ice, rain, and snow mixing ratios and number concentrations are prognostic variables. Rain and snow both require other hydrometeors to already exist, unlike cloud droplets, which form via aerosol activation, and cloud ice, which can form from aerosol and cloud droplet freezing, homogeneously and heterogeneously. Typically, snow and rain hydrometeors are larger and fall faster than cloud particles. Finally, the cumulus category realized for a given environment is a function of dynamically determined entrainment and its cloud phase is based on a temperature threshold. Compared to Cesana et al. (2019), the GISS-ModelE3 version used here includes the following updates pertinent to our findings: depositional growth of stratiform snow, neglected in the original scheme[12], is treated; the Bergeron enhancement employed in the original scheme[12], which transfers water directly from cloud droplets to cloud ice, is omitted and the process instead only mediated through the vapor phase, as in nature; at supercooled temperatures, heterogeneous ice nucleation occurs only in the immersion mode, using the temperature dependence of Demott et al. (2010). Another update is that these GISS-ModelE3 simulations have finer layering in the middle and upper troposphere, and a higher top at 0.002 hPa. The primary structural difference between the Phys version and the Tun1-3 configurations is an alternative formulation for convective entrainment. For the findings presented here, the impact of the entrainment change is merely indirect, in that it coincidentally enables the overall climatological skill requirement to be met using developers'-choice default values of uncertain stratiform microphysical coefficients, rather than those determined by the objective approach for Tun1-3.

Text S3:

We modified a few other elements of the lidar simulator to make it more consistent with GISS-ModelE3. First, to be consistent with the definition of effective radius (Foot, 1988) we modified the default bulk ice density from 500 to 917 kg/m^3, which is used for all frozen hydrometeors. This modification reduces and increases the lidar simulator cloud fraction at the top and the bottom of the high clouds (not shown). Then, the ice particle shape in the lidar calculation is set to nonspherical, which also increases the cloud fraction of ice clouds (not shown). Finally, we slightly modified the discrimination line used to distinguish ice and liquid cloud pixels in the CALIPSO-GOCCP and lidar simulator cloud phase diagnostic (Cesana and Chepfer, 2013) to classify ice particles with a large total attenuated backscatter (ATB) that follow the ice parameterized line but are located below the discrimination line (see supplementary Fig. 10a). These occurrences may be more frequent in GISS-ModelE3 than in the ESM used by Cesana and Chepfer (2013) because GISS-ModelE3 has a higher vertical resolution and includes contribution from snow.

Text S4:

The first case study was derived from observations during the Atmospheric Radiation Measurement (ARM) West Antarctic Radiation Experiment (AWARE) (Silber et al., 2019). We note that greater ice formation rates in GISS-ModelE3 Phys than estimated from observations (Silber et al., 2020) correspond to less liquid water optical depth than observed, which we obtained by changing the ice nucleation scale factor parameter from 0.1 to 8. This modification allows us to probe the simulator capability to “see through” optically thinner liquid layers, which are common over polar regions (Silber et al., 2020). The second case study corresponds to the Small Particles in Cirrus (SPARTICUS) case (Muhlbauer et al., 2014), which represents an anvil cirrus cloud system at midlatitudes over the Southern Great Plains (SGP). Note that we did not change any model cloud parameters for the SPARTICUS case.

Text S5:

We quantify ESM cloud feedbacks (Fig. 4) using an International Satellite Cloud Climatology Project (ISCCP)-derived radiative kernel method (Zelinka et al., 2016). The cloud feedback is separated into contributions from low (at pressures ≥ 680 hPa, roughly 3 km) and non-low (at pressures < 680 hPa) clouds and further decomposed into amount, altitude, optical depth, and residual contributions (Supplementary Fig. 11 and Tables 1 and 2). The amount, altitude and optical depth contributions quantify the feedback generated by changes in cloud fraction, altitude and optical depth, respectively, while keeping the other two parameters constant in the cloud top pressure and optical depth ISCCP bin space. The ISCCP-derived radiative kernel method and its shortcomings are described in Zelinka et al. (2012b). The main shortcoming of this method comes from the residual when decomposing the cloud feedback into amount, altitude and optical depth contributions. One must be careful when analyzing the different contributions if the residual is of the same order of magnitude.

Here we aim to characterize the atmospheric contributions to cloud feedbacks by prescribing the SST in the control experiment, based on monthly observations, and by applying a uniform warming of 4K in the perturbed experiment (Webb et al., 2017). While the atmospheric-only cloud feedbacks (i.e., using prescribed SST perturbation) do not capture the effect of increased CO_2 and SST-atmosphere coupling, they are representative of the global cloud feedbacks determined from coupled atmosphere-ocean CO2-forced simulations (Ringer et al., 2014). The cloud feedbacks are computed for the constrained configuration of the GISS-ModelE3, Phys (Fig. 4, Supplementary Table 1 and Fig. 11), but also for the three other configurations, Tun1-3 (Supplementary Table 2), to analyze the robustness of the feedbacks in a larger pool of models. We note that the cloud fraction seen by the ISCCP simulator is consistent with the cloud fraction seen by the radiation and the lidar simulator, meaning that when precipitation is neglected in the radiation and the lidar simulator, its contribution to the ISCCP simulator is also neglected.

The CMIP5 and CMIP6 cloud feedback values are from Zelinka et al. (2020) and are computed using different kernels than those used this study but produce very similar results (Zelinka et al., 2012a).

The ECS values in Supplementary Table 3 are from Cesana and Del Genio (2021) and Zelinka et al. (2020). For the CMIP5 and CMIP6 multimodel means (Fig. 4 and Supplementary Table 3), all the results from each modeling center are first averaged, such that each modeling center contributes one data point to the multimodel means to improve model independence.

Supplementary Figures

Figure S1: Total, ice, liquid and undefined-phase cloud profiles (from top to bottom) in the liquid-topped mixed-phase cloud in the Antarctic case. The first column corresponds to the cloud water content from the native GISS-ModelE3 while the second, third and fourth columns correspond to cloud fraction from the lidar simulator outputs with and without precipitation and the difference, respectively.

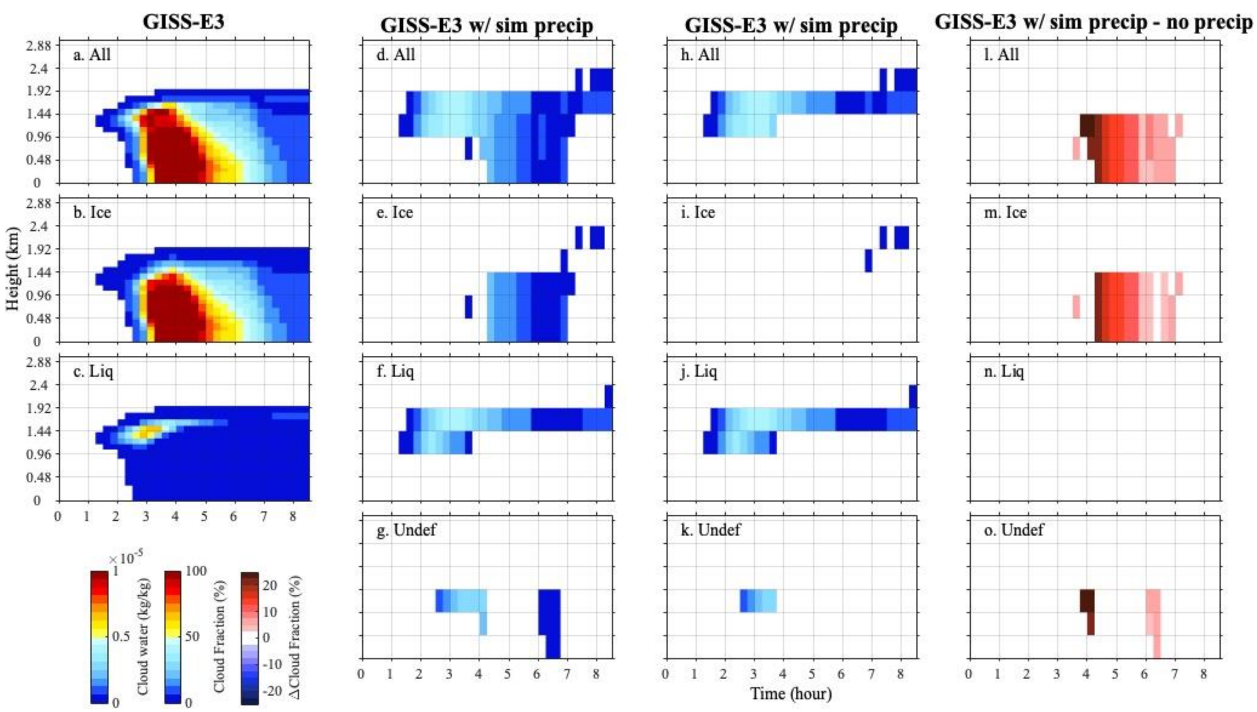

Figure S2: Same as Figure S1 for the stratiform cirrus case over the southern great plains. Note that there are no undefined-phase clouds in this case.

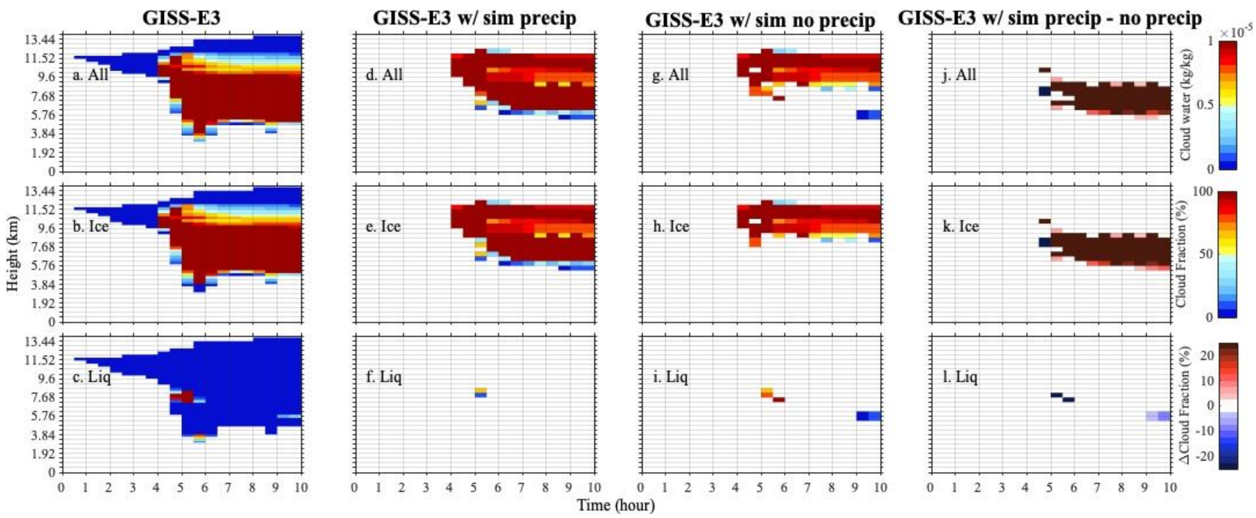

Figure S3: Zonal profiles (x axis, latitude, N; y axis, altitude, km) of the lidar simulator GISS-ModelE3 outputs without precipitation (a), the difference between with and without (b), the difference between with large-scale frozen precipitation and without precipitation (c) and the difference between with large-scale rain and without precipitation (d). Note that no changes occur between panel b and c in the high levels and that the color scale of panel d is smaller than that of panel c.

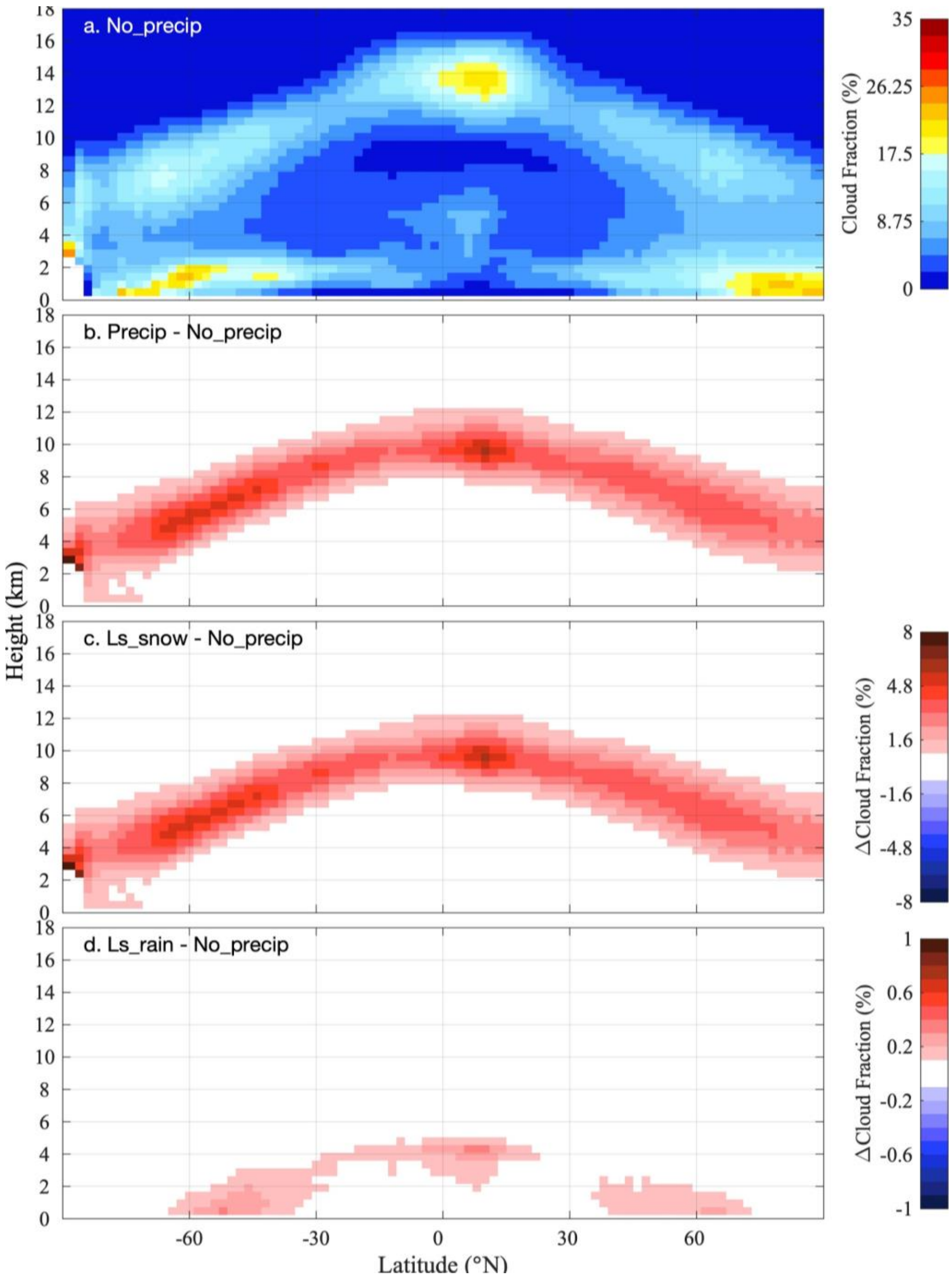

Figure S4: Zonal profiles (x axis, latitude, N; y axis, altitude, km) of CALIPSO-GOCCP observations and the lidar simulator GISS-ModelE3 outputs with precipitation (top) and the difference between with and without precipitation for the four different GISS-ModelE3 configurations: Phys and Tun1 to 3, from left to right.

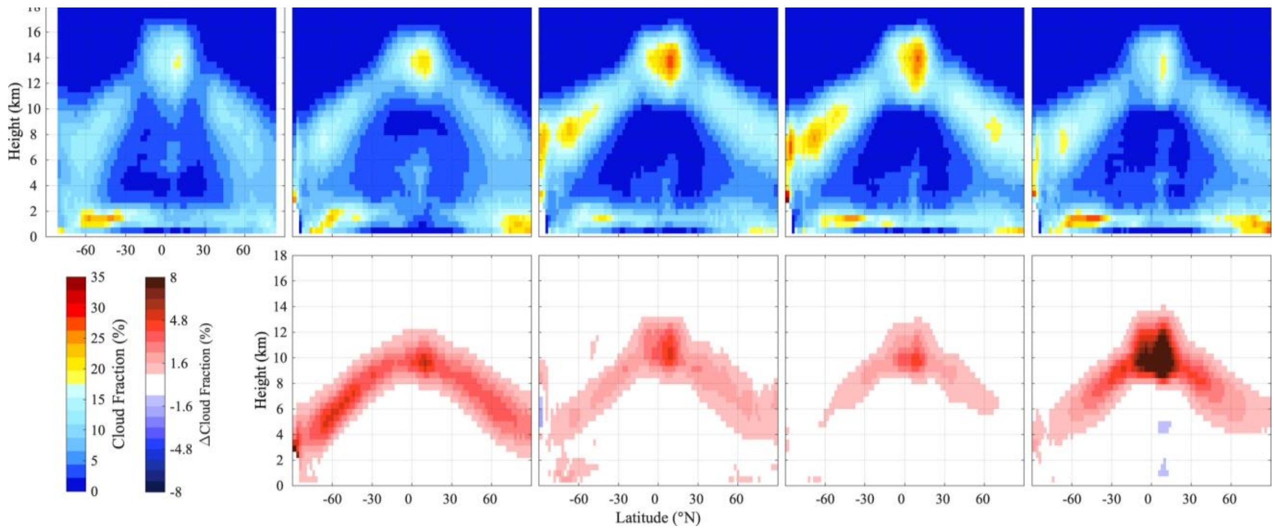

Figure S5: Zonal profiles (x axis, latitude, N; y axis, altitude, km) of CALIPSO-GOCCP observations (top) and GISS-ModelE3 bias of the total, ice, liquid and undefined-phase cloud fractions for the four different GISS-ModelE3 configurations with precipitation using the lidar simulator, from the second row to the bottom row, Phys and Tun1 to 3.

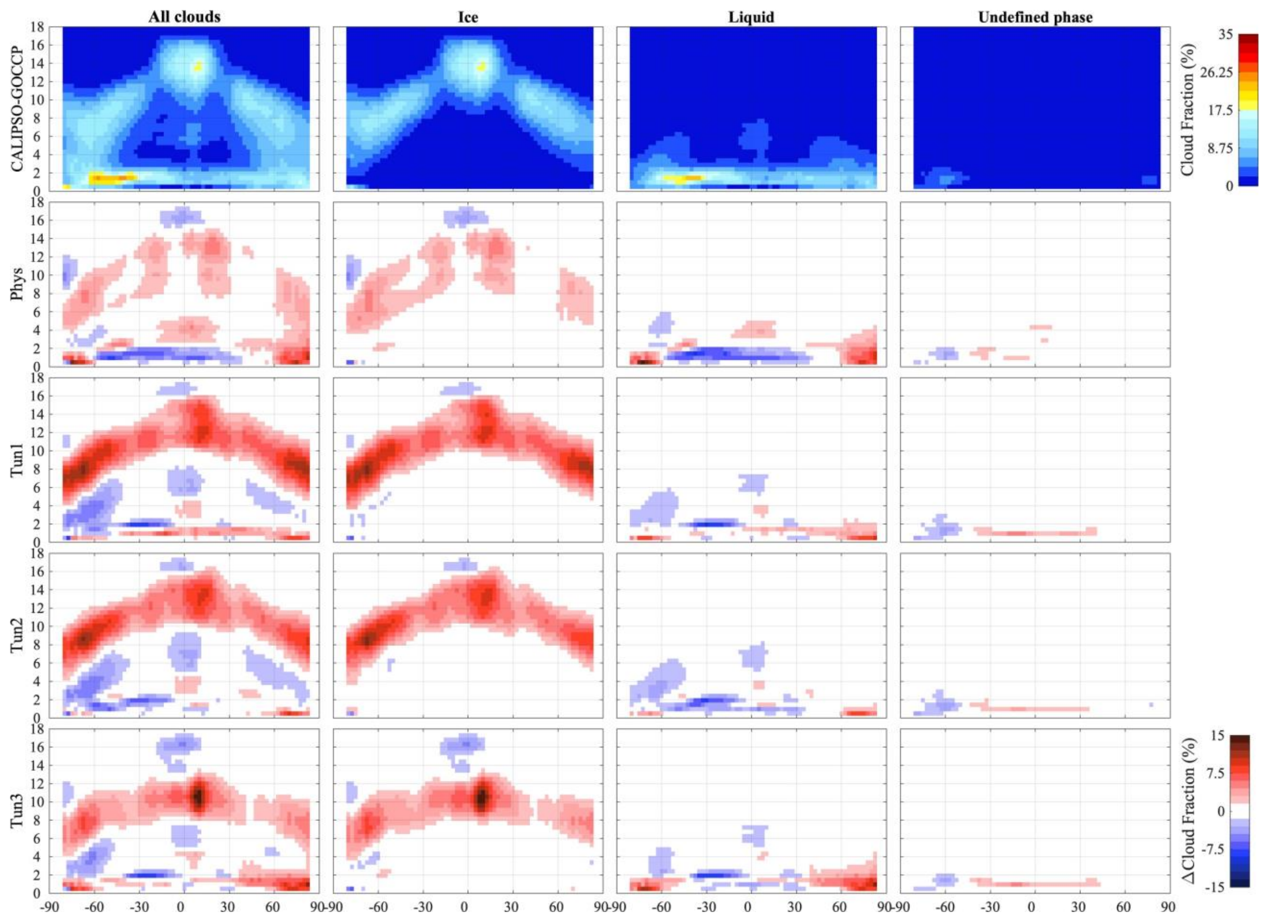

Figure S6: Effect of the precipitation on the relation between temperature (y axis, °C) and frequency supercooled condensate fraction (SCF, x axis). This figure emphasizes the variability of the relationship among the GISS-ModelE3 different configurations with (solid) and without (dotted) precipitation (the specific names of each version are shown in the legend). The CALIPSO-GOCCP observation frequency SCF is shown in black (2007-2016 Nighttime v2.9).

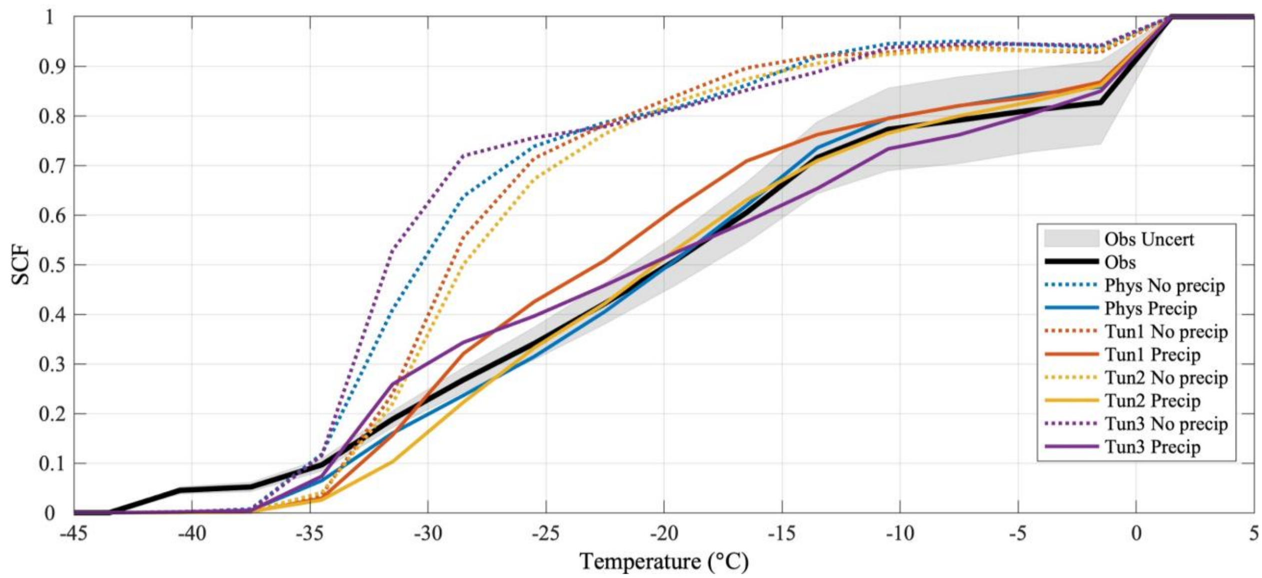

Figure S7: Zonal altitude (km, left) and temperature (˚C, right) profiles of frequency SCF. The CALIPSO-GOCCP observations are shown on the top row (2007-2016 Nighttime v2.9) while the lidar simulator GISS-ModelE3 outputs with and without precipitation correspond to the middle and bottom rows, respectively. The black and green dashed lines correspond to the 50 % liquid and ice iso contours of the observations and the simulations, respectively.

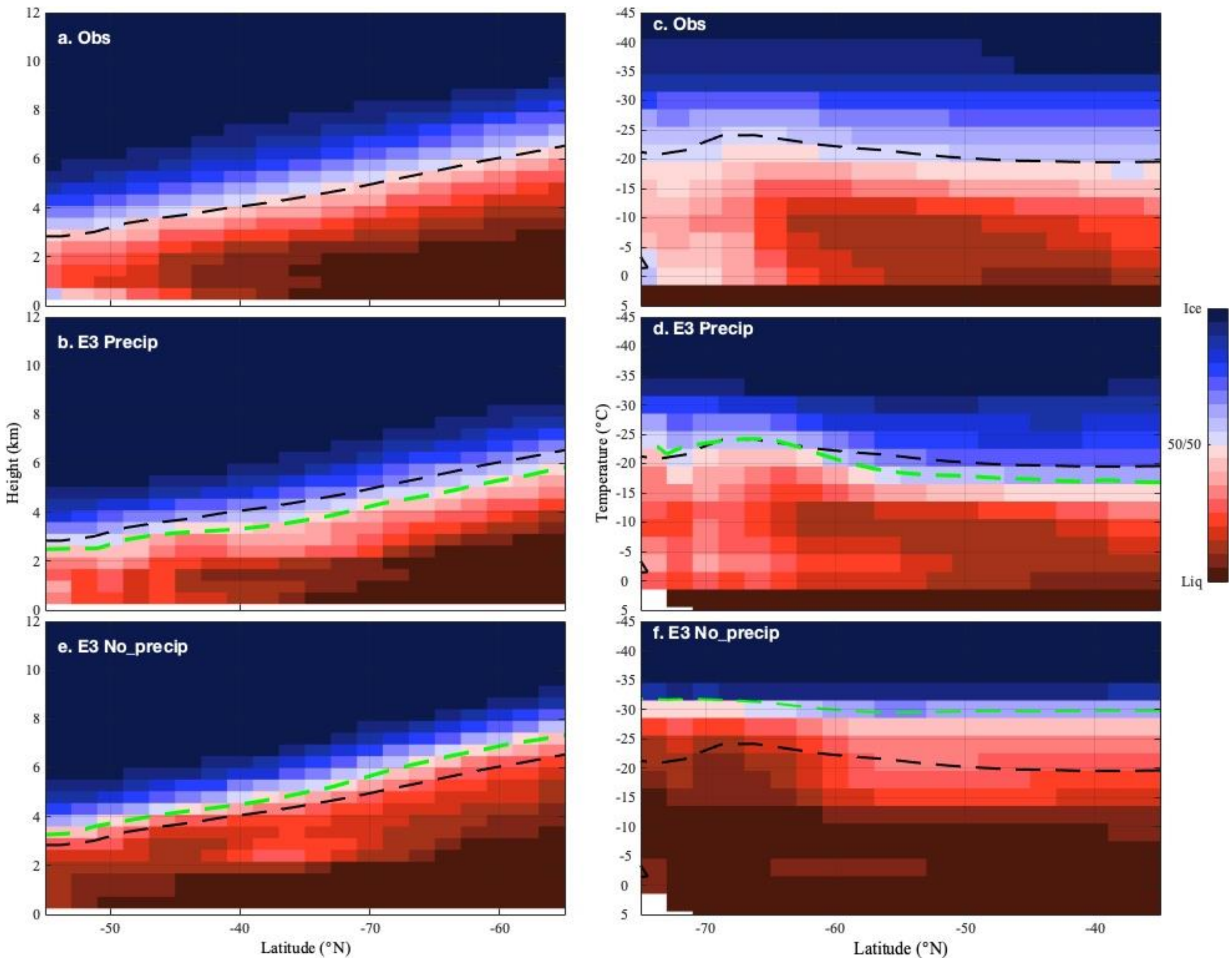

Figure S8: Zonal mean of net, SW and LW cloud radiative effect at the top of the atmosphere. The net, LW and SW CRE are represented in black, red and blue with (solid lines) and without (dotted lines) the effect of large-scale precipitation for GISS-ModelE3 Phys. The area-weighted global averages are shown in the legend.

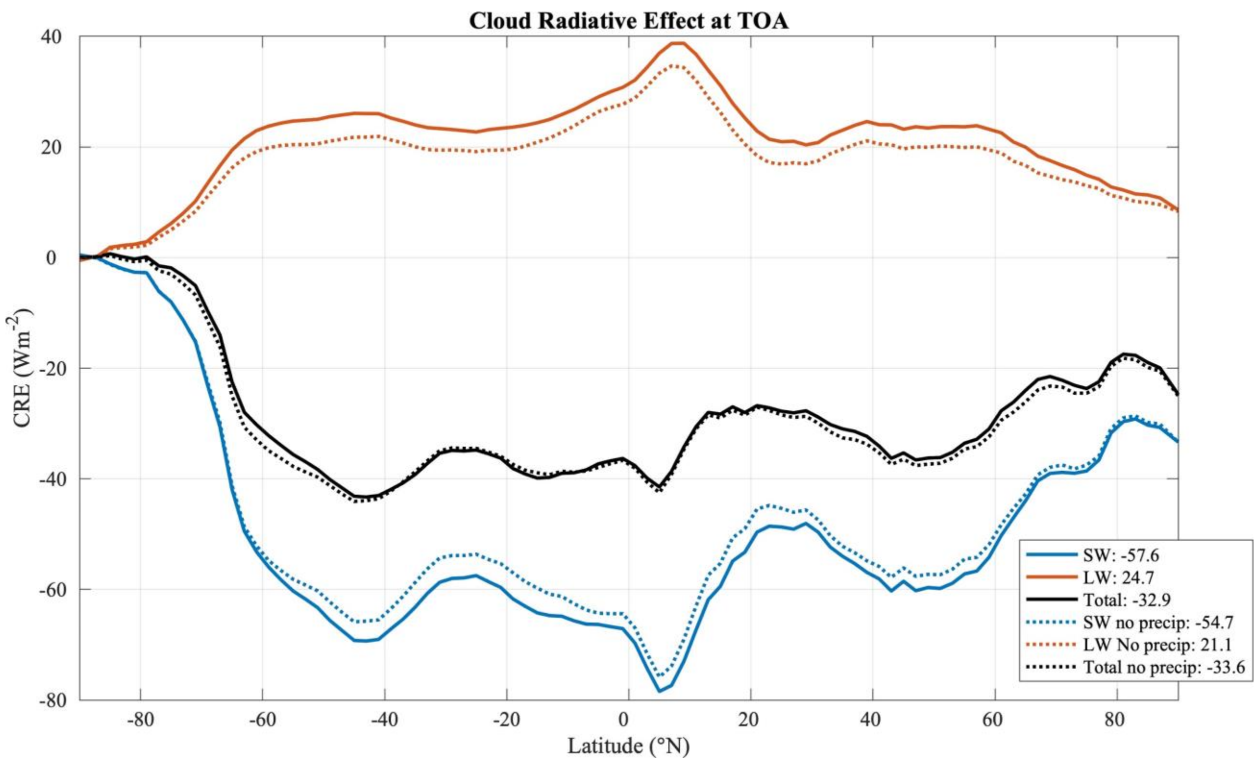

Figure S9: Schematic of the effect of making precipitation visible to the radiation scheme in GISS-ModelE3. In response to global warming, ice crystals transition to water droplets globally. However, depending on the region of the globe, cloud properties may respond differently to global warming. For example, in the tropics (left), the amount and optical depth of non-low clouds (at heights > 3 km) decrease, a process that is enhanced by making precipitation visible to radiation since cloud ice becomes scarcer and produces less snow. As a result, both cloud ice and snow decrease, contributing to strengthen the SW positive feedback (less SW radiation reflected back to space) and weaken the LW positive feedback (more surface LW cooling). Over the Arctic (right), the cloud amount and optical depth increase while the snow amount decreases, for the reasons mentioned above. As a consequence, adding precipitation slightly offset the increase in cloud amount and optical depth seen by radiation, thereby weakening the SW negative feedback (less SW radiation reflected back to space) with negligible effect in the LW.

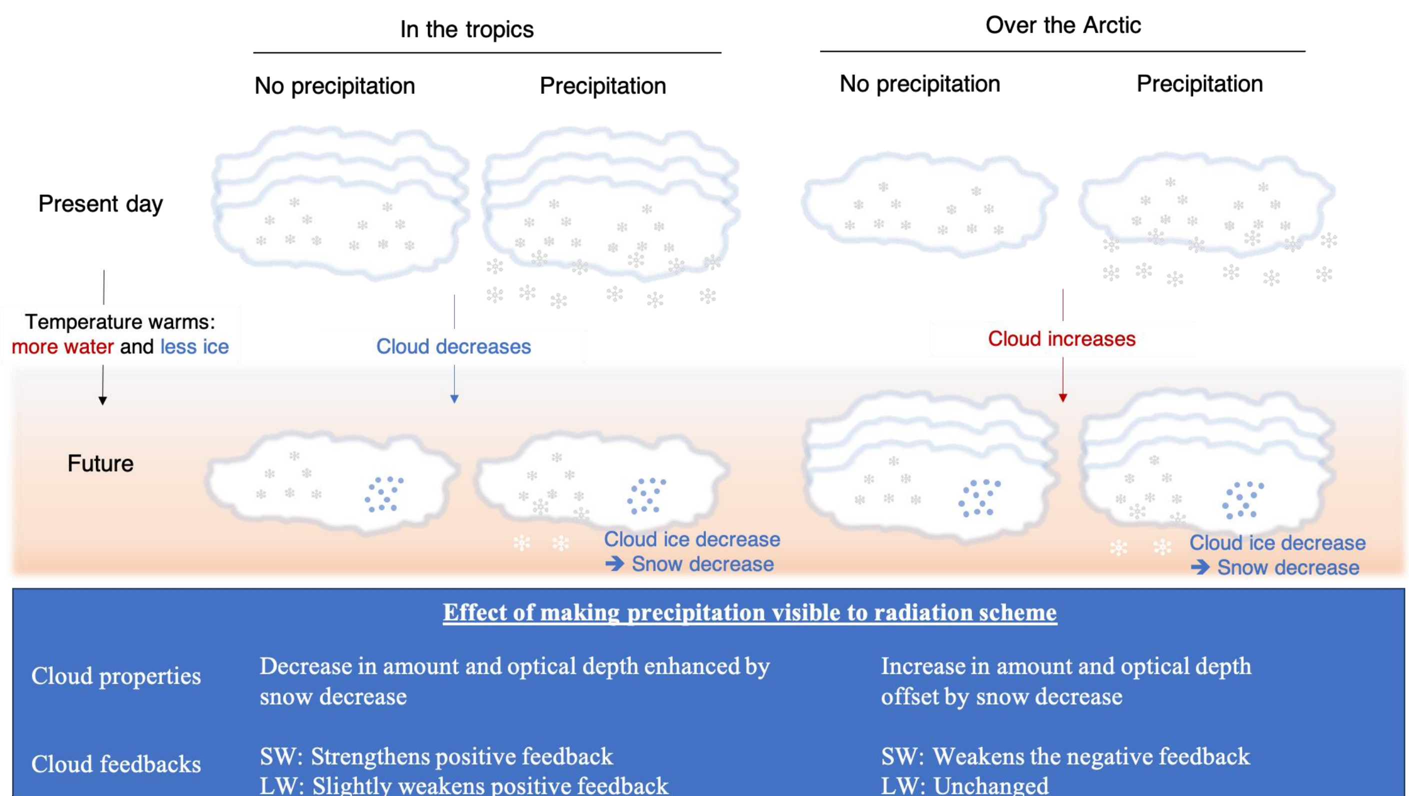

Figure 10: Phase diagram for the (a) SGP cirrus cloud case and Antarctica mixed-phase cloud case using GISS-ModelE3. The color shading represents the number of cloudy pixels as a function of the perpendicular attenuated total backscatter (ATBper, y-axis, km^{-1} sr^{-1}) and the attenuated total backscatter (ATBtot, x-axis, km^{-1} sr^{-1}) as in Cesana and Chepfer (2013). The solid black line corresponds to the original discrimination line used in the lidar simulator while the dashed black line is the modified version used in GISS-ModelE3 to account for ice paarticles with a large ATB signature, e.g., the pixels between the two black lines in the upper panel.

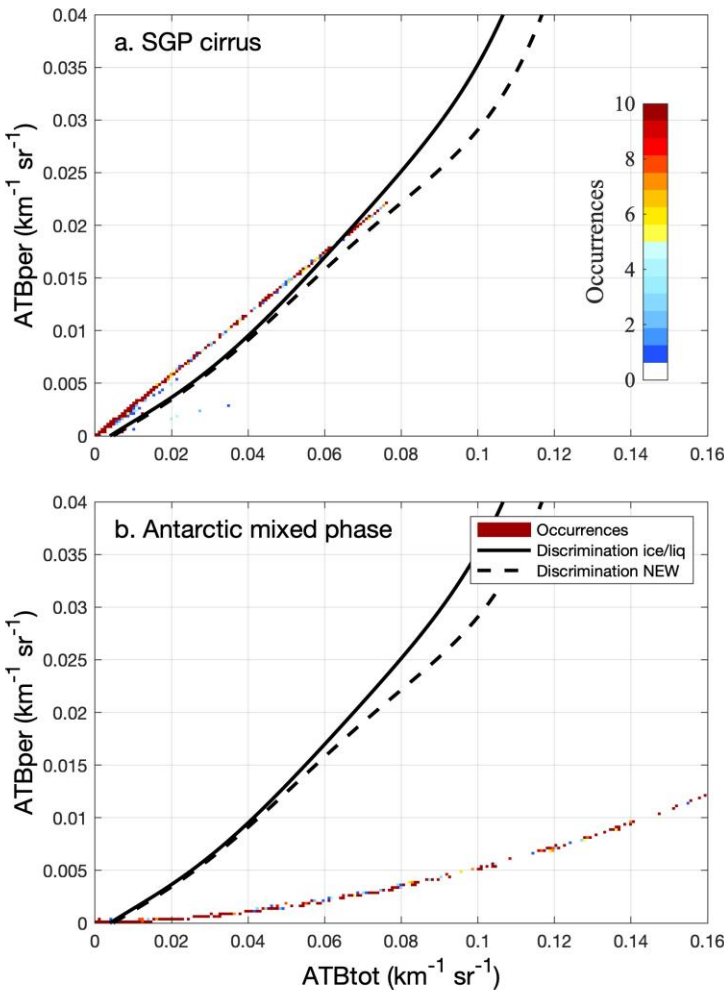

Figure S11: Effect of precipitation on cloud feedbacks (left to right) for different types of feedbacks for GISS-ModelE3 Phys. The first row represents zonal means of standard net, LW and SW cloud feedbacks ($Wm^{-2}K^{-1}$; left to right) for all (black), non-low (blue) and low (red) clouds. The second, third and fourth rows show further decomposition into total (black), altitude (purple), optical depth (orange) and amount (green) contributions for all, non-low and low clouds, respectively. The simulations with and without large-scale frozen precipitation are represented by solid and dotted lines, respectively. Note that the corresponding area-weighted global averages are shown in Supplementary Table 1.

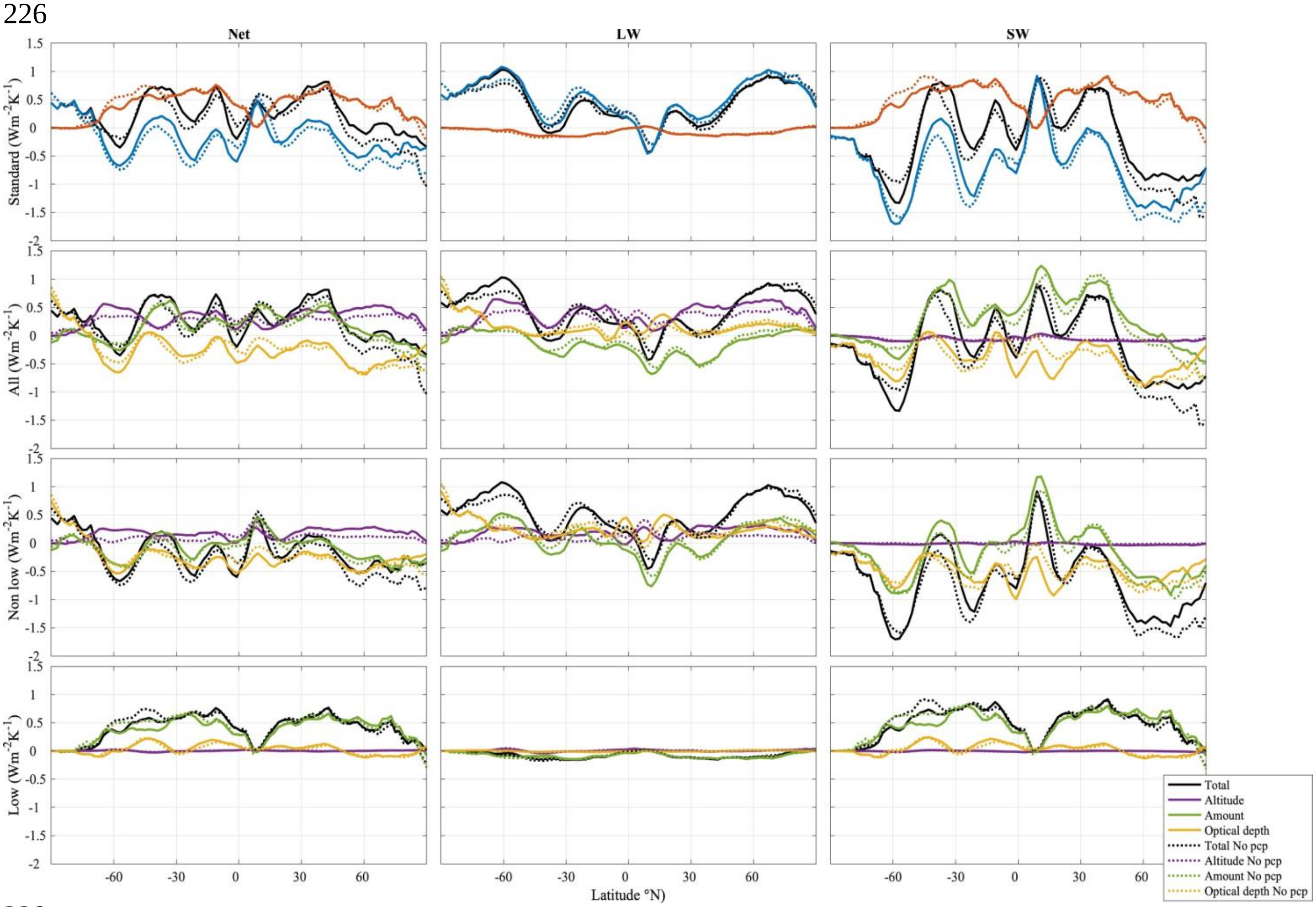

Supplementary Tables

Table S1: Effect of snow on cloud feedback. Global mean net, LW and SW total cloud feedbacks ($Wm^{-2}K^{-1}$) and their non-low and low contributions further divided into altitude, amount and optical depth components for GISS-ModelE3 (configuration Phys) using Zelinka et al.(Zelinka et al., 2016) kernels along with amip and amip-p4K experiments. Note that the zonal means of the altitude, amount and optical depth contributions for all, non-low and low clouds are shown in Figure S11. Differences that are smaller or equal to the internal variability are shown in grey.

		Net			LW			SW		
		Ctrl	No_pcp	Δ	Ctrl	No_pcp	Δ	Ctrl	No_pcp	Δ
All	**total**	**0.26**	**0.14**	**0.12**	**0.44**	**0.47**	**-0.03**	**-0.19**	**-0.33**	**0.14**
	altitude	0.36	0.29	0.07	0.42	0.35	0.07	-0.06	-0.06	0
	amount	0.16	0.11	0.05	-0.15	-0.09	-0.06	0.31	0.19	0.12
	Optical depth	-0.26	-0.28	0.02	0.16	0.17	-0.01	-0.42	-0.44	0.02
Non low	**total**	**-0.14**	**-0.28**	**0.14**	**0.52**	**0.55**	**-0.03**	**-0.66**	**-0.83**	**0.17**
	altitude	0.2	0.12	0.08	0.21	0.13	0.08	-0.02	-0.01	-0.01
	amount	-0.08	-0.14	0.06	0.07	0.14	-0.07	-0.16	-0.28	0.12
	Optical depth	-0.25	-0.26	0.01	0.24	0.28	-0.04	-0.49	-0.54	0.05
Low	**total**	**0.4**	**0.42**	**-0.02**	**-0.08**	**-0.08**	**0**	**0.48**	**0.5**	**-0.02**
	altitude	0	0	0	0.01	0.01	0	0	0	0
	amount	0.39	0.41	-0.02	-0.08	-0.09	0.01	0.47	0.5	-0.03
	Optical depth	0.02	0.02	0	0	0	0	0.02	0.02	0

Table S2: **Effect of snow on cloud feedback across all configurations**. Same as Table 1 but averaged over the four GISS-ModelE3 configurations (Phys and Tun1-3). Note that, as in the GISS-ModelE3 phys configuration used in the main manuscript, the total net cloud feedback roughly doubles when the precipitation is seen by radiation.

		Net			LW			SW		
		Ctrl	No_pcp	Δ	Ctrl	No_pcp	Δ	Ctrl	No_pcp	Δ
	total	**0.21**	**0.11**	**0.10**	**0.46**	**0.46**	**-0.01**	**-0.25**	**-0.35**	**0.10**
All	altitude	0.34	0.27	0.06	0.40	0.33	0.07	-0.06	-0.06	-0.01
	amount	0.15	0.12	0.03	-0.14	-0.10	-0.03	0.28	0.22	0.06
	Optical depth	-0.28	-0.29	0.01	0.17	0.19	-0.02	-0.45	-0.48	0.03
	total	**-0.18**	**-0.28**	**0.10**	**0.52**	**0.52**	**0.00**	**-0.70**	**-0.80**	**0.10**
Non low	altitude	0.17	0.11	0.07	0.18	0.11	0.07	-0.01	-0.01	-0.01
	amount	-0.06	-0.07	0.02	0.06	0.09	-0.03	-0.12	-0.16	0.04
	Optical depth	-0.27	-0.28	0.01	0.30	0.36	-0.06	-0.57	-0.64	0.06
	total	**0.38**	**0.39**	**-0.01**	**-0.06**	**-0.06**	**0.00**	**0.45**	**0.45**	**-0.01**
Low	altitude	0.01	0.01	0.00	0.01	0.01	0.00	-0.01	-0.01	0.00
	amount	0.37	0.38	0.00	-0.07	-0.07	0.00	0.44	0.45	-0.01
	Optical depth	0.03	0.03	0.00	0.00	0.00	0.00	0.02	0.03	-0.01

Table S3: **List of CMIP5 (left) and CMIP6 (right) models used in this study along with their equilibrium climate sensitivities.** The models marked with a star include the effect of large-scale precipitation in their radiation schemes. The modeling center mean is shown on the rightmost column of each side.

CMIP5 Models	ECS (K) Model Mean	Center Mean
ACESS1.0	3.85	3.69
ACCESS1-3*	3.53	
BCC-CSM1-1-m	2.89	2.87
BCC-CSM1-1	2.84	
BNU-ESM	4.04	
CanESM2	3.70	
CCSM4	2.94	
CSIRO-Mk3-6-0*	4.09	
CNRM-CM5	3.25	
GFDL-ESM2G	2.43	2.95
GFDL-ESM2M	2.44	
GFDL-CM3	3.99	
GISS-E2-R	2.12	2.22
GISS-E2-H	2.31	
HadGEM2-ES*	4.58	
INMCM4	2.08	
IPSL-CM5A-LR	4.13	3.62
IPSL-CM5B-MR	4.11	
IPSL-CM5B-LR	2.61	
MIROC5	2.71	3.68
MIROCESM	4.64	
MPI-ESM-MR	3.45	3.51
MPI-ESM-P	3.46	
MPI-ESM-LR	3.63	
MRI-CGCM3	2.61	
NorESM1-M	2.81	2.90
NorESM1-ME	2.98	
Multimodel Mean	3.29	
Multimodel STD	0.69	
Multimodel Mean precip*	4.07	
Multimodel STD precip*	0.53	

CMIP6 Models	ECS (K) Model Mean	Center Mean	
ACCESS-CM2*	4.66	4.66	4.28
ACCESS-ESM1-5	3.89	3.89	
BCC-CSM2-MR	3.02	3.14	
BCC-ESM1	3.26		
CAMS-CSM1-0	2.29	2.29	
CanESM5	5.64	5.64	
CESM2*	5.15	4.95	
CESM2-FV2*	5.16		
CESM2-WACCM*	4.68		
CESM2-WACCM-FV2*	4.8		
CNRM-CM6-1	4.9	4.67	
CNRM-CM6-1-HR	4.33		
CNRM-ESM2-1	4.79		
E3SM-1-0*	5.31	5.31	
EC-Earth3*	4.33	4.33	
EC-Earth3-Veg*	4.33		
GFDL-CM4	3.89	3.27	
GFDL-ESM4	2.65		
GISS-E2-1-G	2.71	2.75	
GISS-E2-1-H	3.12		
GISS-E2-2-G	2.43		
HadGEM3-GC31-LL*	5.55	5.45	
HadGEM3-GC31-MM*	5.44		
UKESM1-0-LL*	5.36		
INM-CM4-8	1.83	1.88	
INM-CM5-0	1.92		
IPSL-CM6A-LR	4.56	4.56	
MIROC-ES2L	2.66	2.63	
MIROC6	2.6		
MPI-ESM-1-2-HAM	2.95	2.99	
MPI-ESM1-2-HR	2.98		
MPI-ESM1-2-LR	3.03		

Multimodel Mean no LS precip	3.1
Multimodel STD no LS precip	0.53

MRI-ESM2-0	3.13	3.13	
NorCPM1	3.03	3.03	2.69
NorESM2-LM*	2.56	2.53	
NorESM2-MM*	2.49		
SAM0-UNICON*	3.72	3.72	
Multimodel Mean	3.76		
Multimodel STD	1.16		
Multimodel Mean precip*	4.42		
Multimodel STD precip*	1.02		
Multimodel Mean no LS precip	3.37		
Multimodel STD no LS precip	1.05		

Reference

Cesana, G., Chepfer, H., Winker, D., Getzewich, B., Cai, X., Jourdan, O., et al., (2016), Using in situ airborne measurements to evaluate three cloud phase products derived from CALIPSO, *Journal of Geophysical Research*, *121*(10), 5788–5808. https://doi.org/10.1002/2015JD024334

Cesana, Grégory, & Chepfer, H., (2013), Evaluation of the cloud thermodynamic phase in a climate model using CALIPSO-GOCCP, *Journal of Geophysical Research: Atmospheres*, *118*(14), 7922–7937. https://doi.org/10.1002/jgrd.50376

Cesana, Grégory, Del Genio, A. D., Ackerman, A. S., Kelley, M., Elsaesser, G., Fridlind, A. M., et al., (2019), Evaluating models' response of tropical low clouds to SST forcings using CALIPSO observations, *Atmospheric Chemistry and Physics*, *19*(5), 2813–2832. https://doi.org/10.5194/acp-19-2813-2019

DeMott, P. J., Prenni, A. J., Liu, X., Kreidenweis, S. M., Petters, M. D., Twohy, C. H., et al., (2010), Predicting global atmospheric ice nuclei distributions and their impacts on climate, *Proceedings of the National Academy of Sciences of the United States of America*, *107*(25), 11217–11222. https://doi.org/10.1073/pnas.0910818107

Foot, J. S., (1988), Some observations of the optical properties of clouds. II: Cirrus, *Quarterly Journal of the Royal Meteorological Society*, *114*(479), 145–164. https://doi.org/10.1002/qj.49711447908

Gettelman, A., & Morrison, H., (2015), Advanced two-moment bulk microphysics for global models. Part I: Off-line tests and comparison with other schemes, *Journal of Climate*, *28*(3), 1268–1287. https://doi.org/10.1175/JCLI-D-14-00102.1

Muhlbauer, A., Kalesse, H., & Kollias, P., (2014), Vertical velocities and turbulence in midlatitude anvil cirrus: A comparison between in situ aircraft measurements and ground-based Doppler cloud radar retrievals, *Geophysical Research Letters*, *41*(22), 7814–7821. https://doi.org/10.1002/2014GL062279

Ringer, M. a, Andrews, T., & Webb, M. J., (2014), Ocean Climate Change Experiments, *5*(ii), 1–8. https://doi.org/10.1002/2014GL060347.Received

Silber, I., Fridlind, A. M., Verlinde, J., Ackerman, A. S., Chen, Y. S., Bromwich, D. H., et al., (2019), Persistent Supercooled Drizzle at Temperatures Below −25 °C Observed at McMurdo Station, Antarctica, *Journal of Geophysical Research: Atmospheres*, *124*(20), 10878–10895. https://doi.org/10.1029/2019JD030882

Silber, I., Fridlind, A. M., Verlinde, J., Russell, L. M., & Ackerman, A. S., (2020), Nonturbulent Liquid-Bearing Polar Clouds: Observed Frequency of Occurrence and Simulated Sensitivity to Gravity Waves, *Geophysical Research Letters*, *47*(10), 1–11. https://doi.org/10.1029/2020GL087099

Smith, R. N. B., (1990), A scheme for predicting layer clouds and their water content in a general circulation model, *Quarterly Journal of the Royal Meteorological Society*, *116*(492), 435–460. https://doi.org/10.1002/qj.49711649210

Webb, M. J., Andrews, T., Bodas-Salcedo, A., Bony, S., Bretherton, C. S., Chadwick, R., et al., (2017), The Cloud Feedback Model Intercomparison Project (CFMIP) contribution to CMIP6, *Geoscientific Model Development*, *10*(1), 359–384. https://doi.org/10.5194/gmd-10-359-2017

Wilson, D. R., & Ballard, S. P., (1999), A microphysically based precipitation scheme for the UK meteorological office unified model, *Quarterly Journal of the Royal Meteorological Society*, *125*(557), 1607–1636. https://doi.org/10.1002/qj.49712555707

Zelinka, M. D., Klein, S. A., & Hartmann, D. L., (2012a), Computing and Partitioning Cloud Feedbacks Using Cloud Property Histograms. Part I: Cloud Radiative Kernels, *Journal of Climate*, *25*(11), 3715–3735. https://doi.org/10.1175/jcli-d-11-00248.1

Zelinka, M. D., Klein, S. A., & Hartmann, D. L., (2012b), Computing and partitioning cloud feedbacks using cloud property histograms. Part II: Attribution to changes in cloud amount, altitude, and optical depth, *Journal of Climate*, *25*(11), 3736–3754. https://doi.org/10.1175/JCLI-D-11-00249.1

Zelinka, M. D., Zhou, C., & Klein, S. A., (2016), Insights from a refined decomposition of cloud feedbacks, *Geophysical Research Letters*, *43*(17), 9259–9269. https://doi.org/10.1002/2016GL069917